Supplementary Information

Construction of Mn-Zn binary carbonate microspheres on interconnected rGO networks: motivating an atomic-scale bimetallic synergy on enhancing lithium storage properties

Songju Ruan,[a] Ao Xiao,[a] Zhufeng Zheng,[a] Cheng Ma,[a] Xiaojun Liu,[a] Jitong Wang,[ab] Wenming Qiao[ab] and Licheng Ling*[ab]*

[a] State Key Laboratory of Chemical Engineering, East China University of Science and Technology, Shanghai 200237, China.

[b] Key Laboratory of Specially Functional Polymeric Materials and Related Technology, East China University of Science and Technology, Shanghai 200237, China

[*] Corresponding author: wangjt@ecust.edu.cn; lchling@ecust.edu.cn

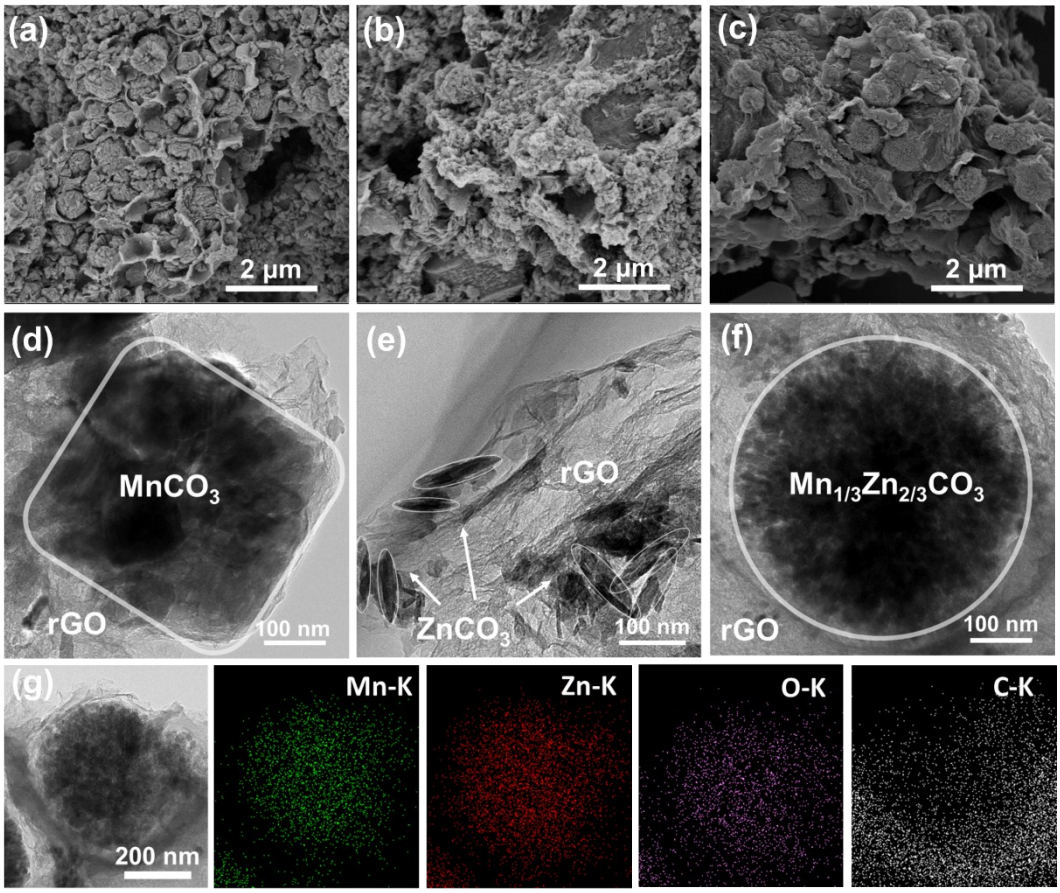

Fig. S1. FE-SEM images of (a) M3Z0G, (b) M0Z3G and (c) M1Z2G; TEM images of (d) M3Z0G, (e) M0Z3G and (f) M1Z2G; (g) Elemental mapping images of M1Z2G.

As shown in FE-SEM images, some fragment of crystals could be detected in **Fig. S1a-b** while the structure of $Mn_{1/3}Zn_{2/3}CO_3$ microspheres (**Fig. S1c**) seem to be more robust, which could result in the difference in the cycling stability of electrodes. The different micro morphologies of these samples are further observed in TEM images. The pure $MnCO_3$ display a cubic shape with a crystal size of 450 nm as shown in **Fig. S1d**. The needle-like $ZnCO_3$ crystals exhibit a small crystal size of 100 nm in length (**Fig. S1e**). The $Mn_{1/3}Zn_{2/3}CO_3$ has a microsphere shape with a diameter of 500 nm (**Fig. S1f**). The elemental mapping images of M1Z2G display the

uniform distribution of Mn, Zn, O and C in the composites (**Fig. S1g**). It is obvious that the spots representing the elements of Mn and Zn shows a spherical shape, corresponding to the microsphere observed in the TEM image, which provides evidence for success synthesis of the single-phase mixed carbonates. The spots of C could be detected in area of graphene, revealing the interrelation between graphene and crystals.

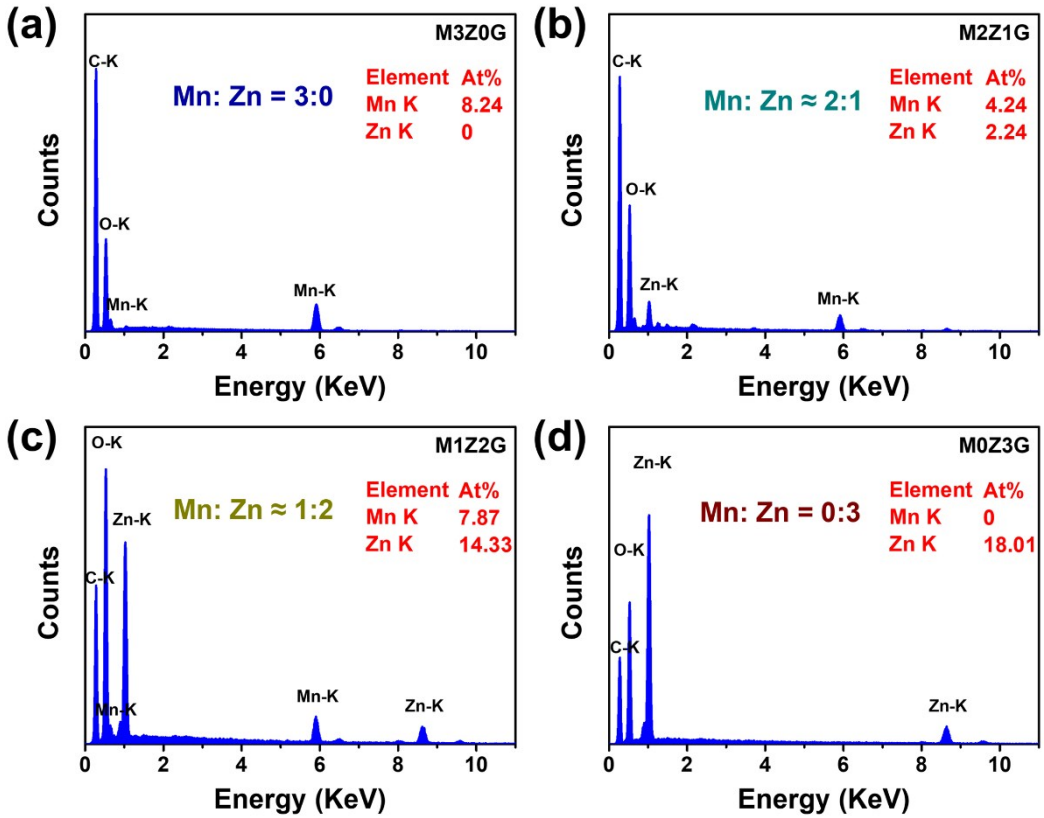

Fig. S2. EDS spectrum of (a)M3Z0G, (b)M2Z1G, (c)M1Z2G and (d) M0Z3G.

Table S1. The results of ICP measurements.

Sample	Elements	Mass (%)	Atom ratio (%, Actual)	Atom ratio (%, Designed)
M2Z1G	Mn	22.9	65.6	66.6
	Zn	14.3	34.4	33.3
M1Z2G	Mn	11.0	31.3	33.3
	Zn	28.7	68.7	66.6

In spite of uncontrollable loss during the experiment, the atom ratio of Mn and Zn is approaching the added ratio of $MnSO_4$ and $ZnSO_4$. (**Fig. S2**) The ICP measurements give the accurate atom content of Mn and Zn among total metal elements, which is close to the designed values. The difference may be caused by system errors. The results of EDS analysis and ICP measurements give supports for the Vegard's law fitting in the main text.

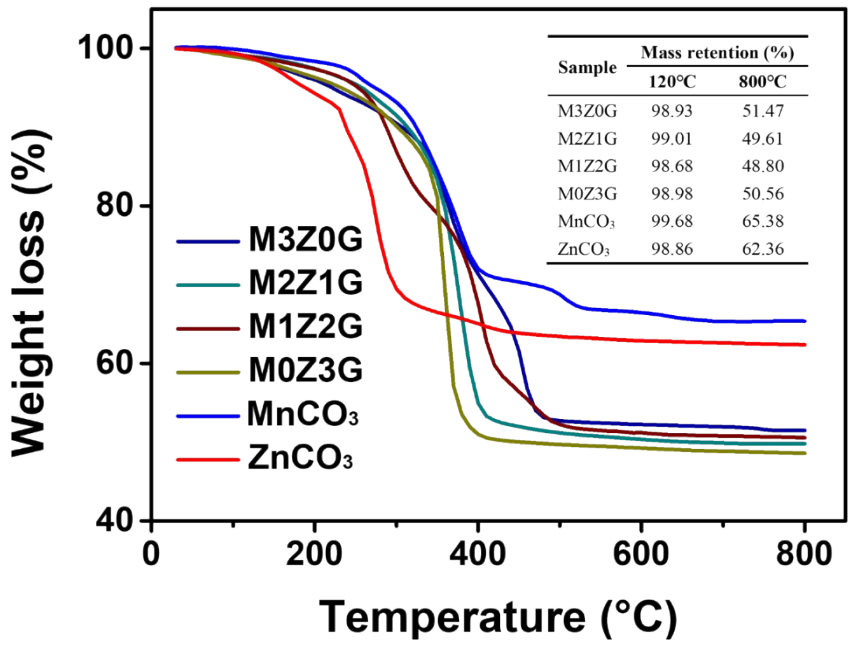

Fig. S3. TGA curves of MZGs in air.

The content of graphene is determined by TGA as shown in **Fig. S3**. The TGA curves of pure $MnCO_3$ and $ZnCO_3$ are also offered for reference. The mass loss before 120 ℃ primarily originates from the removal of adsorbed water. After eliminating the influence of water, the mass ratios of carbonates are calculated as 79.3%, 77.4%, 77.0% and 81.0% for M3Z0G, M2Z1G, M1Z2G and M0Z3G, respectively. That means the content of graphene is similar for four composites, which is around 20%.

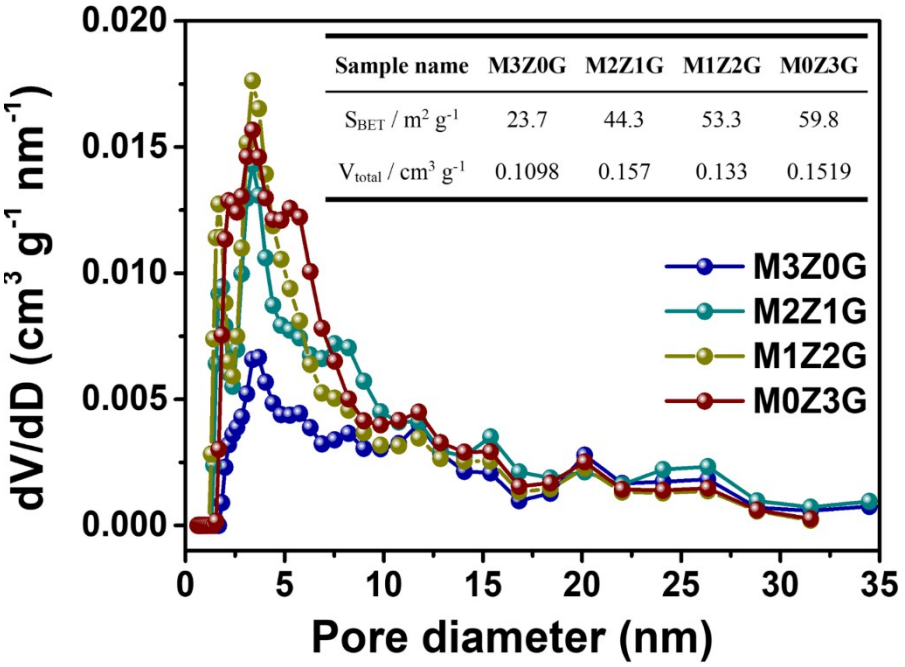

Fig. S4. DFT pore distribution and pore volume of MZGs.

The DFT pore size distributions of all samples almost center on 4 to 5 nm (**Fig. S4**), which mainly result from the assembly of graphene nanosheets. The mesoporous structure could accelerate permeation of electrolyte and provide accessible channels for better diffusion kinetics of Li^+.

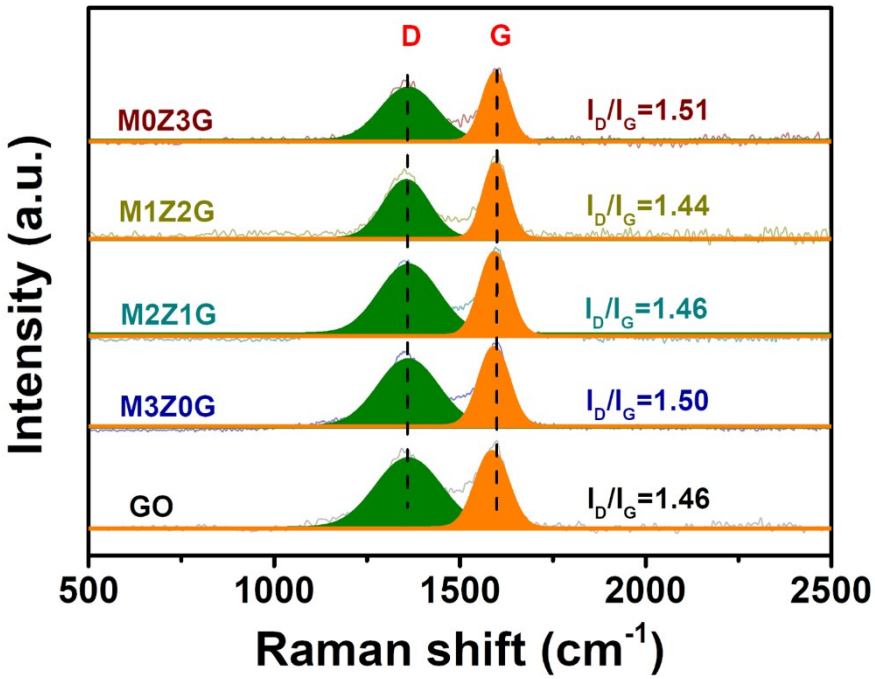

Fig. S5. Raman spectra of original graphene oxides and MZGs.

The two dominant peaks, namely D-band on 1350 cm^{-1} and G-band on 1600 cm^{-1}, correspond to the disordered carbon and graphite carbon on graphene, respectively. The intensity of these two peaks are too strong to detect the existence of carbonates. The area ratio of D/G (I_D/I_G) of four composites does not show significant difference, which is approaching the value of raw GO.

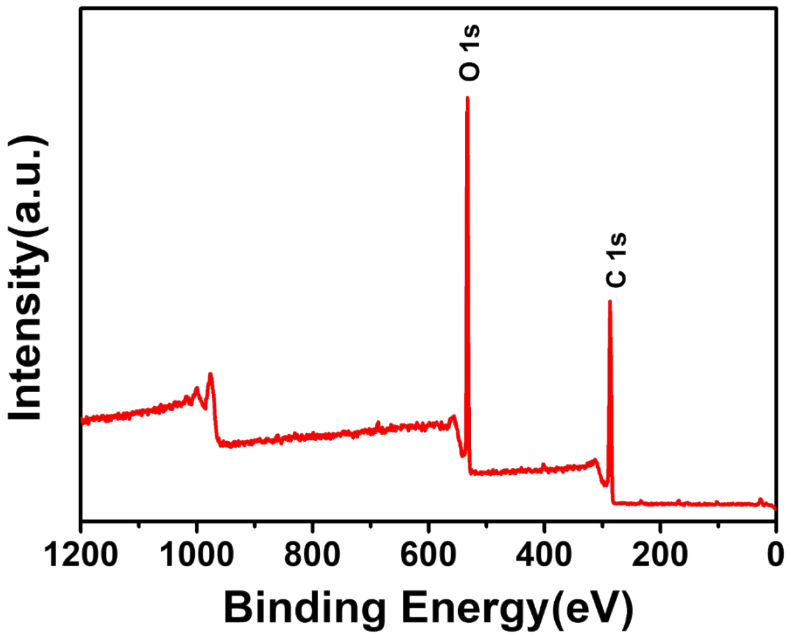

Fig. S6. XPS spectra of original graphene oxides.

The full scan of XPS indicates the high purity of original graphene oxides.

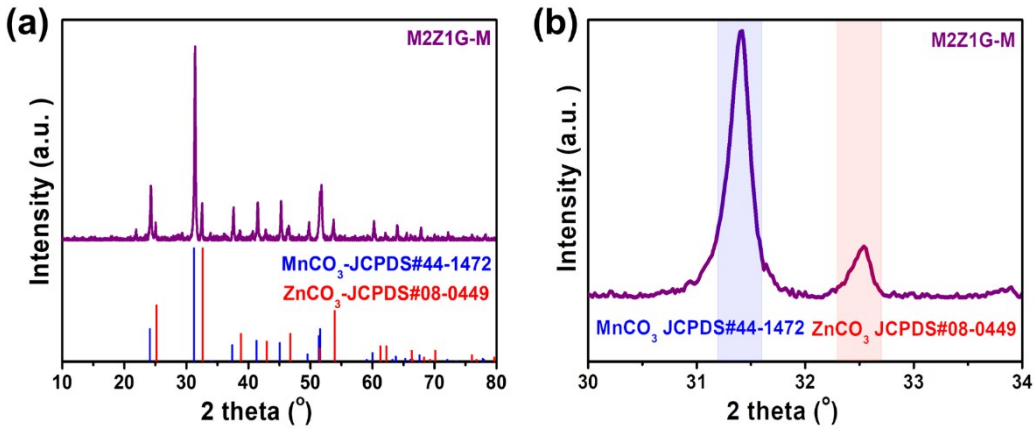

Fig. S7. (a) XRD patterns of M2Z1G-M; (b)The 104 Bragg peak of M2Z1G-M.

The two separated 104 peaks could be detected in the XRD patterns of the mixed carbonates prepared by the mechanical mixing. By contrast with MZGs, it proves that the mixed metal carbonates synthesized in this paper is a single-phase crystal.

Table S2. The calculated lattice fringe spacing.

Sample	Interplanar spacing (Å)									
	d_{012}	d_{104}	d_{110}	d_{113}	d_{202}	d_{024}	d_{116}	d_{122}	d_{214}	d_{300}
$MnCO_3$ JCPDS#44-1472	3.6670	2.8500	2.3950	2.1780	2.0050	1.8337	1.7670	1.5375	1.4560	1.3828
M3Z0G	3.6591	2.8467	2.3916	2.1752	2.0019	1.8304	1.7648	1.5354	1.4536	1.3807
M2Z1G	3.6289	2.8198	2.3757	2.1597	1.9839	1.8175	1.7421	1.5200	1.4376	1.3696
M1Z2G	3.5996	2.7851	2.3455	2.1350	1.9654	1.7938	1.7266	1.5031	1.4257	1.3564
M0Z3G	3.5575	2.7510	2.3265	2.1110	1.9481	1.7739	1.7072	1.4933	1.4126	1.3434
$ZnCO_3$ JCPDS#08-0449	3.5500	2.7500	2.3270	2.1110	1.9460	1.7760	1.7030	1.4930	1.4110	1.3430

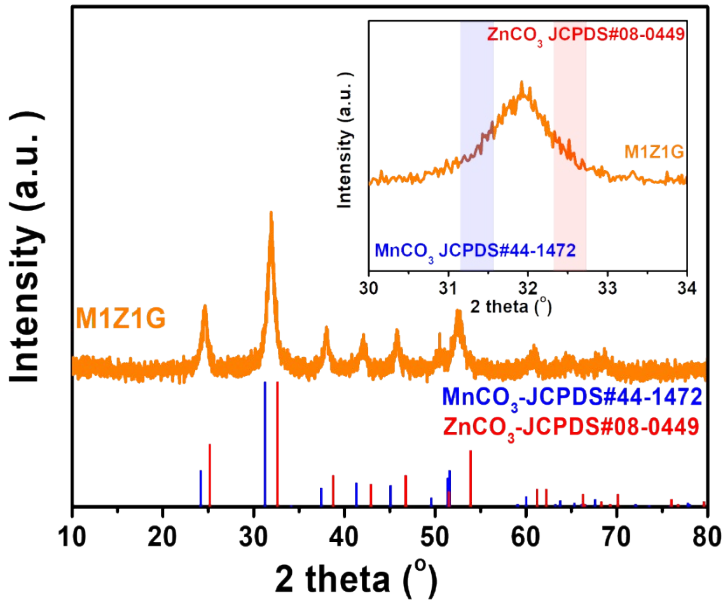

Fig. S8. XRD patterns of M1Z1G.

Table S3. The lattice parameters of M1Z1G.

Parameters	***a*** **(Å)**	***c*** **(Å)**	***v*** **(Å^3)**
Experiment value	4.7285	15.3061	296.38
Fitted value	4.7268	15.3937	297.98
Error	0.036%	0.572%	0.540%

The sample with the Mn/Zn ratio of 1:1 (x=0.5) was prepared and the lattice parameters of the sample were calculated from the XRD pattern, as shown in **Fig. S8** and **Table S3**. The experiment value is close to the fitted one, verifying the of reliability the fitted equation.

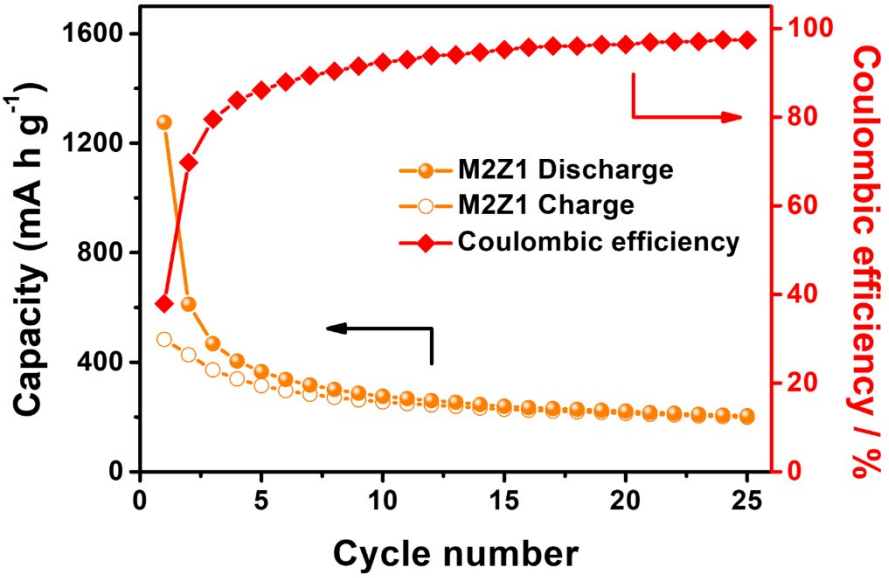

Fig. S9. Cycle performance of M2Z1.

$Mn_{2/3}Zn_{1/3}CO_3$ was prepared via the same procedure as M2Z1G, only excluding the addition of GO. The cycle performance of $Mn_{2/3}Zn_{1/3}CO_3$ is shown in the **Fig. S9**. $Mn_{2/3}Zn_{1/3}CO_3$ could deliver high initial lithium storage capacity but it decreases dramatically after the first cycle. Since the crystals lacks the protection of flexible rGO, electrode pulverization would keep taking place. The low conductivity would reduce the utilization of active materials as well. Therefore, the electrochemical performance of the samples will not be comparable to samples with rGO.

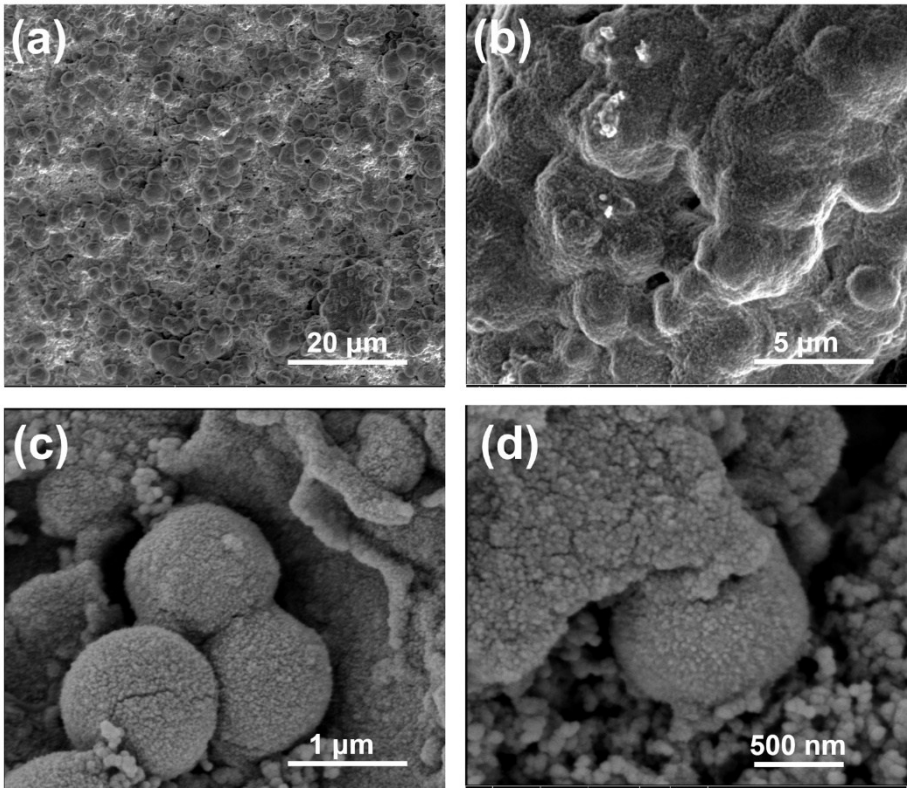

Fig. S10. SEM images of M2Z1G electrodes after 100 cycles.

As shown in **Fig. S10**, there is no obvious pulverization detected on the M2Z1G electrodes after 100 cycles, indicating the good structure during cycling. In other words, the serious volume stress is partly relieved. Despite of the surface-covered SEI film, it could still be seen that the spherical structure of mixed carbonates is well remained, which ensures the stable electrochemical performance of M2Z1G.

Table S4. Rate performance of MZGs

Sample	Reversible capacity (mAh g^{-1}) at various current density (mA g^{-1})						
	200	**500**	**1000**	**2000**	**3000**	**5000**	**200**
M3Z0G	618	507	427	351	296	221	571
M2Z1G	1073	920	784	646	564	431	1071
M1Z2G	383	322	284	245	222	120	464
M0Z3G	413	343	301	260	236	200	406
M2Z1G-M	566	469	378	264	112	47	527

The optimized M2Z1G delivers capacities of 1073, 920, 784, 646, 564 and 431 mAh g^{-1} at current densities of 200, 500, 1000, 2000, 3000, and 5000 mA g^{-1}, respectively. When the current turns back to 200 mA g^{-1}, the composite could also exhibit high capacity of 1072 mAh g^{-1}, indicating the favorable structural stability under high rate.

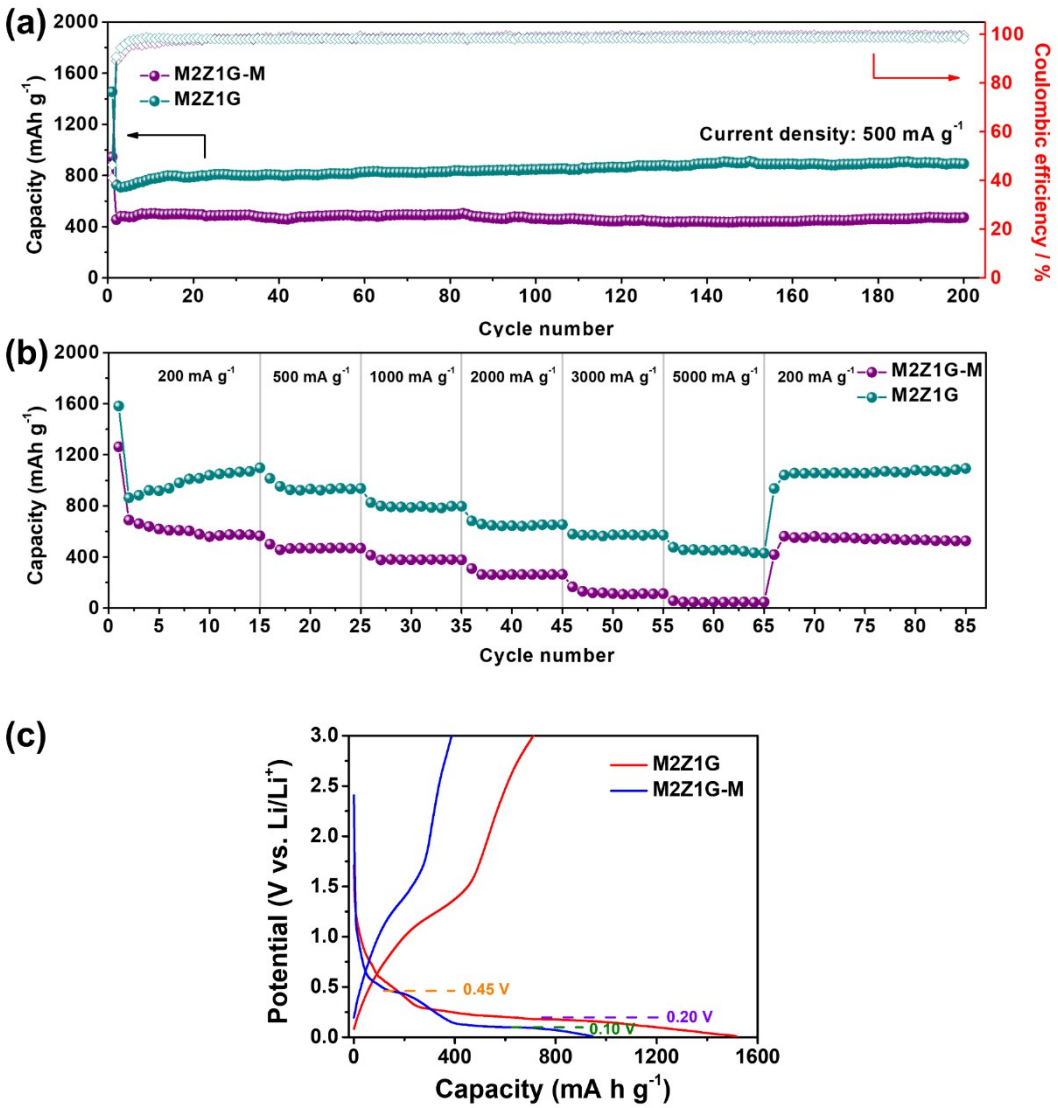

Fig. S11. (a) Cycling performance, (b) Rate capability and (c) Initial discharge/charge curves of M2Z1G-M and M2Z1G.

The electrochemical performance of single-phase M2Z1G is much better than M2Z1G-M, indicating the existence of bimetallic synergy of single-phased mixed carbonates during charging/discharging process. Since the carbonates in M2Z1G is single-phase crystals, there is one long voltage plateau around 0.2 V could be detected on the discharge profile of M2Z1G. However, two separated voltage plateaus at 0.45 V and 0.1 V occur on the discharge profiles

of M2Z1G-M, indicating the lithiation process proceeds in $MnCO_3$ and $ZnCO_3$ respectively. The two types of metal do not show any synergistic effect by simple mixing mechanically.

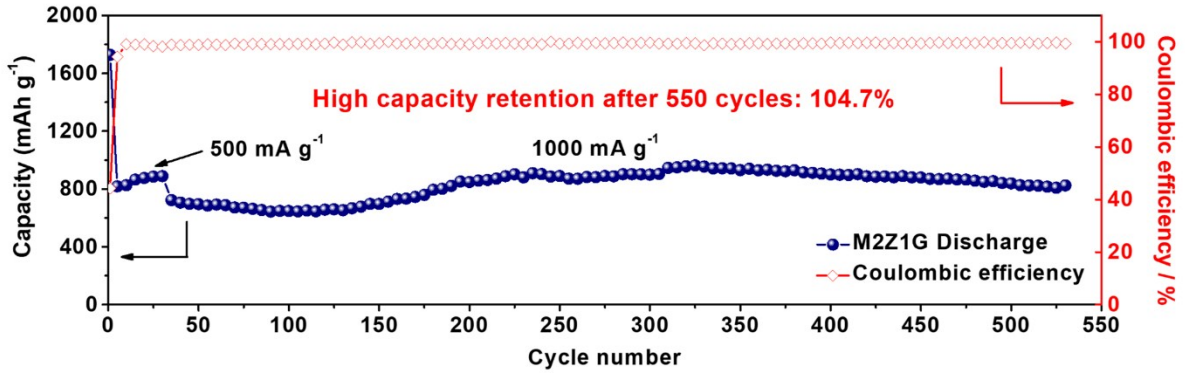

Fig. S12. Cycling performance of M2Z1G at a current density of 1000 mA g^{-1}.

A stable capacity could be maintained with high capacity retention of 104.7% at a rate of 1000 mA g^{-1} for 500 cycles, demonstrating a long cycling life.

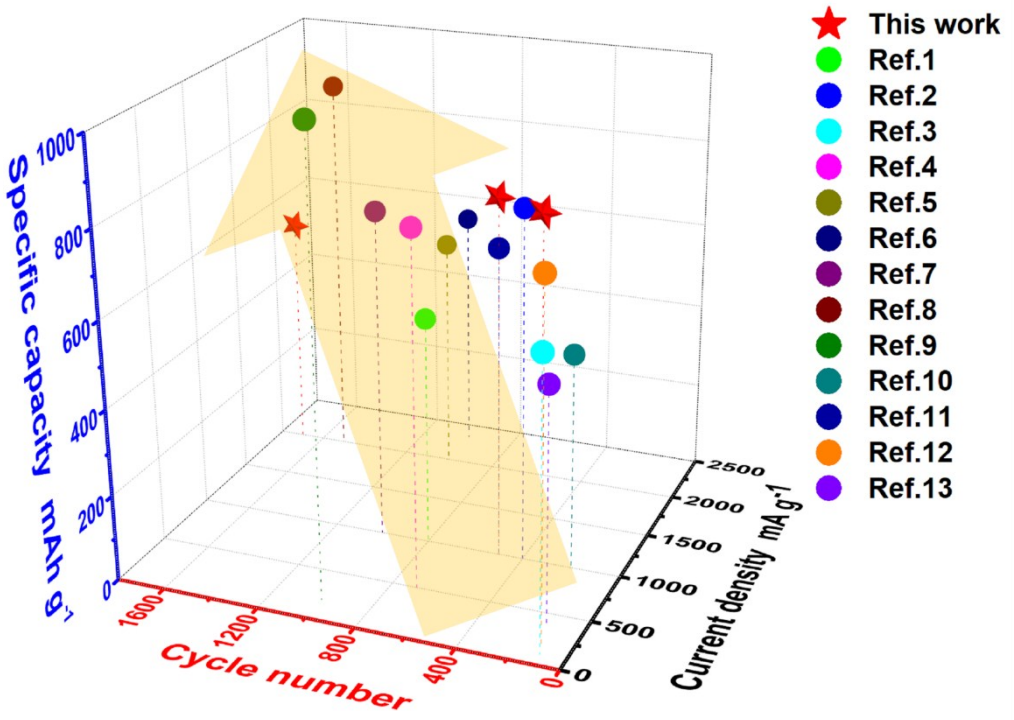

Fig. S13. comparison of the cycling performance of M2Z1G with previous works.

The electrochemical performance of these composites is better or at least comparable to previous $MnCO_3$-based anodes synthesized by relatively complicated process as well as the Mn/Zn-based oxides.

Table S5. Comparison of the electrochemical performances of $Mn_{2/3}Zn_{1/3}CO_3$/rGO prepared in this work with other previous related works

Anode materials	Specific capacity (mAh g^{-1})	Current density (mA g^{-1})	Cycle number	Journal / Reference
$Mn_{2/3}Zn_{1/3}CO_3$/rGO	877	500	200	This work
	825	1000	500	
	550	2000	1700	
$MnCO_3/Mn_3O_4$/rGO	532	1000	800	J. Mater. Chem. A [1]
$MnCO_3$ spindle/GO	807	1000	400	J. Mater. Chem. A [2]
$MnCO_3$ Microsphere	656.8	100	100	ACS Appl. Mater. Interfaces [3]
$MnCO_3$ nanoplates/rGO	811	500	700	Electrochim. Acta [4]
$Ni_{0.25}Mn_{0.75}CO_3$	549	2000	1000	Electrochim. Acta [5]
$Ca_{0.1}Mn_{0.9}CO_3$	568	2335	1000	Chem. Eng. J. [6]
$Mn_xNi_yZn_zCO_3$	760	1000	1000	Small [7]
$Mn_{0.7}Co_{0.3}CO_3$/rGO	900	2000	1500	Adv. Funct. Mater.[8]
Porous $MnCO_3$	1049	200	1000	Nanoscale[9]
$Mn_{0.875}Co_{0.125}CO_3$/CNF	500	1000	200	Electrochim. Acta [10]
Zn_xMnO@carbon hollow disks	713	1000	500	J. Mater. Chem. A [11]
Porous $ZnMn_2O_4$ nanospheres	800	200	120	J. Power Sources [12]
Zn−Mn−O Hollow Microspheres	537	400	150	Langmuir [13]

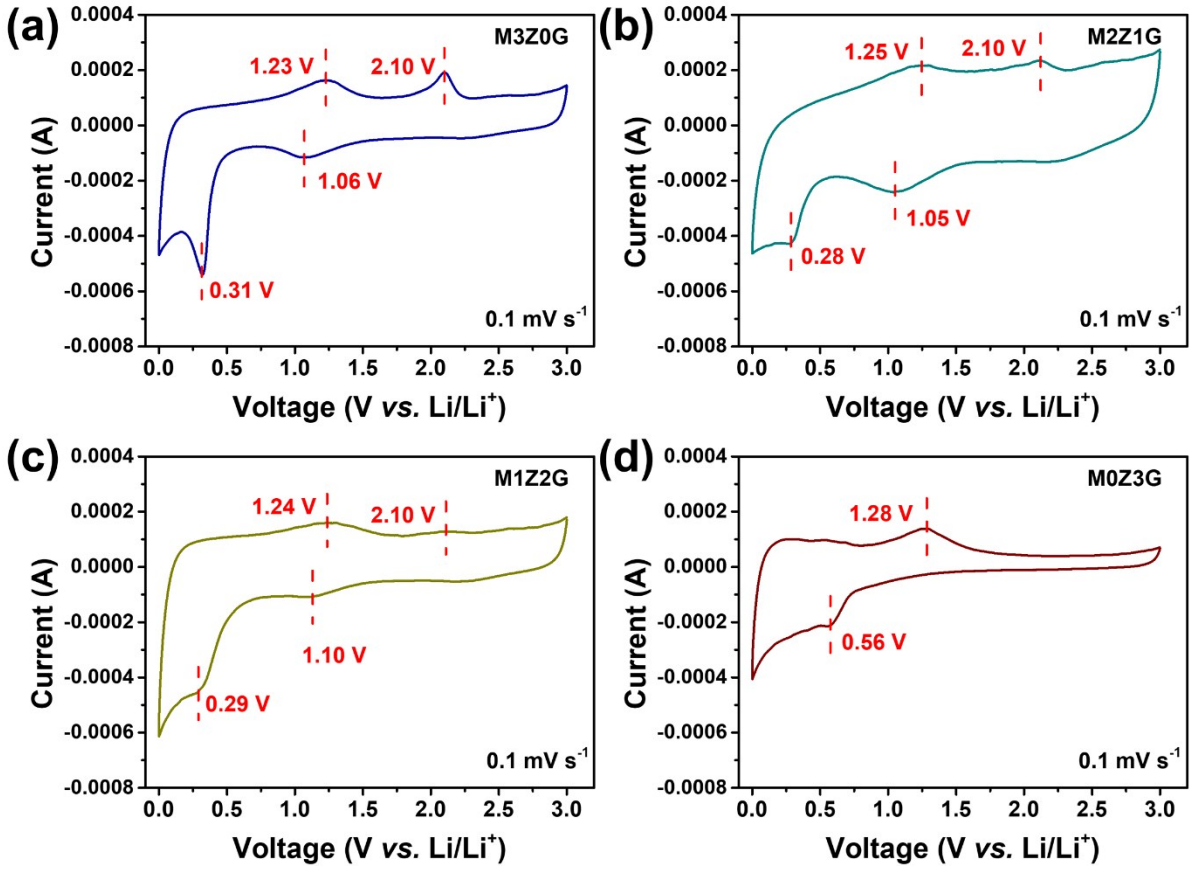

Fig. S14. CV curves of (a) M3Z0G, (b) M2Z1G, (c) M1Z2G and (d) M0Z3G after 200 cycles.

Despite of the slight position shift originating from the electrochemical activation, the main peaks of four composites are still clearly to be distinguished, demonstrating the good reversibility of the electrochemical reaction and high stability of the electrode structure. Moreover, a new pair of shoulders around 2.10/1.10 V corresponding to the conversion reaction between Mn2+/Mnγ+ occur in the curves of mixed carbonates.

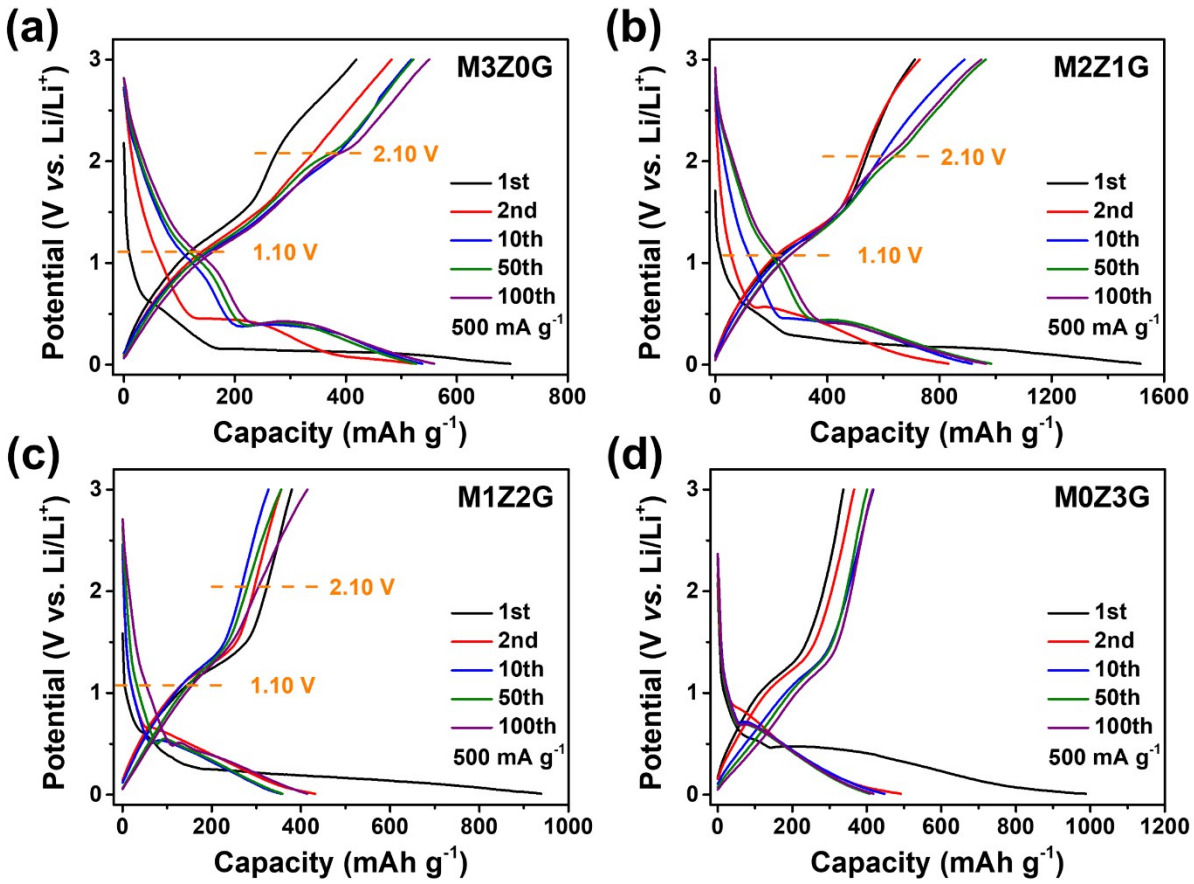

Fig. S15. Galvanostatic discharge/charge profiles of (a) M3Z0G, (b) M2Z1G, (c) M1Z2G and (d) M0Z3G.

By comparing the curves of the 1st, 2nd ,10th, 50th and 100th cycles, it is suggested that the emergence of two general plateaus, located at 1.10 V on discharge curves and 2.10 V on charge curves, respectively, play a critical role in the capacity growth of M3Z1G, M2Z1G and M1Z2G. However, there are no special changes detected in the curves of M0Z3G, indicating the above changes is highly related to the existence of Mn. The results are in good agreement with the above CV analysis.

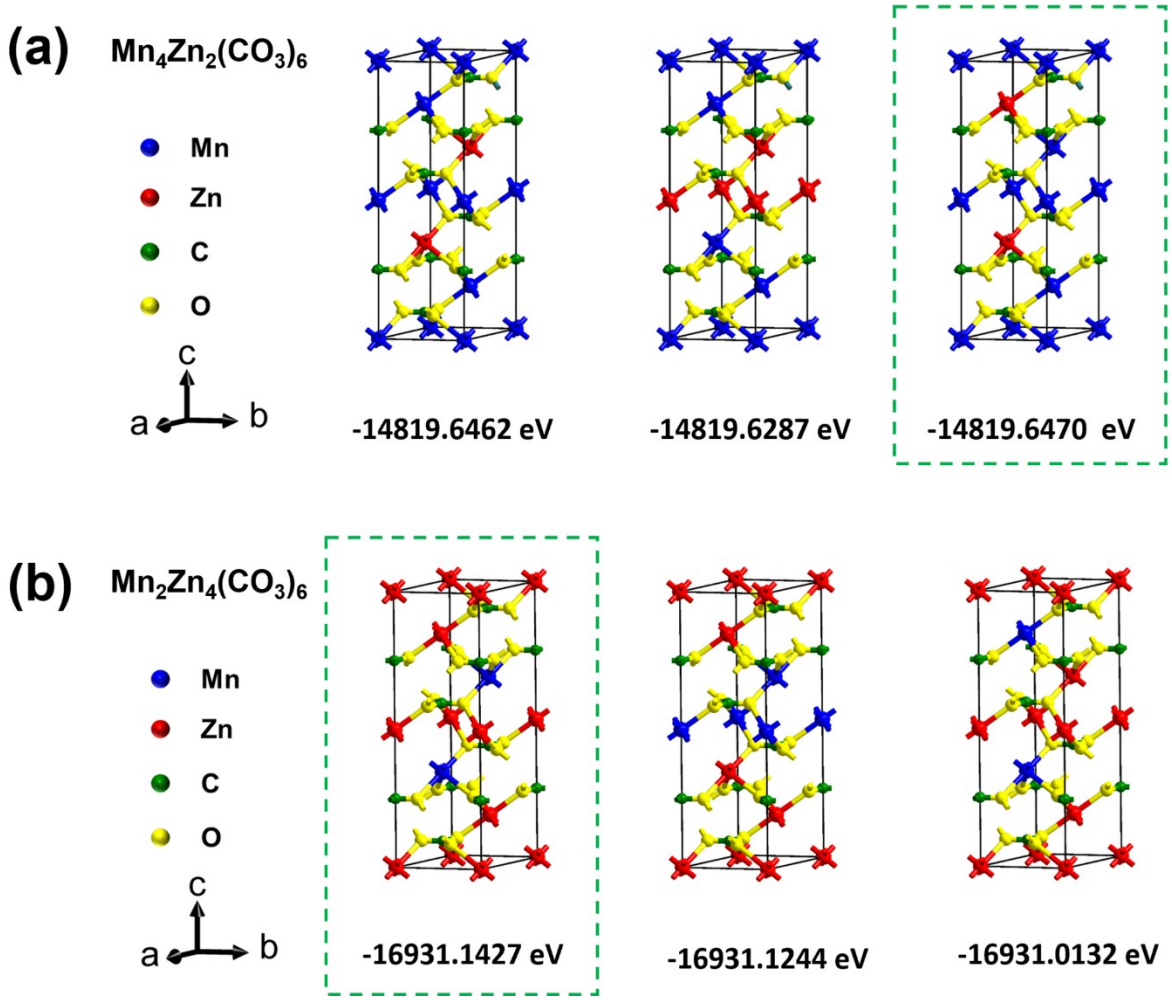

Fig. S16. Possible unit cell structures of (a) $Mn_{2/3}Zn_{1/3}CO_3$ and (b) $Mn_{1/3}Zn_{2/3}CO_3$.

The selected crystal structure has minimum energy so that they would be in the majority of the final crystal. It is more convincing to employ these structures to conduct further DFT calculation.

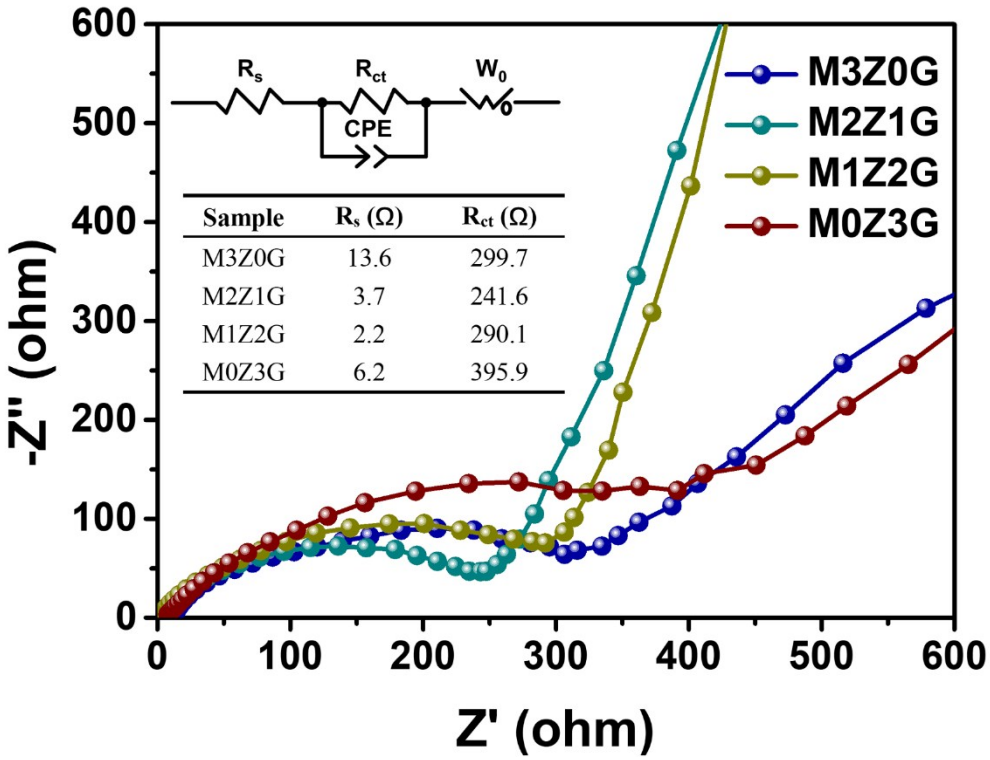

Fig. S17. Nyquist plots of MZGs.

As the equivalent circuit shown in the **Fig. S18**, Rs represents the ohmic resistance, R_{ct} is due to the charge transfer resistance, and Wo is the Warburg resistance related to the Li^+ diffusion. M2Z1G has the smallest charge transfer resistance due to the smallest value of band gap of $Mn_{2/3}Zn_{1/3}CO_3$. The experimental results are in good agreement with DFT calculation.

Reference

1. R. Zhang, D. Wang, L.-C. Qin, G. Wen, H. Pan, Y. Zhang, N. Tian, Y. Zhou and X. Huang, *Journal of Materials Chemistry A*, 2017, **5**, 17001-17011.
2. S. Zhao, F. Feng, F. Yu and Q. Shen, *Journal of Materials Chemistry A*, 2015, **3**, 24095-24102.
3. X. Liang, S. Wang, Y. Wang, M. Wen, B. Deng, D. Qu, Z. Z. Xie and J. Liu, *Acs Applied Materials & Interfaces*, 2016, **8**, 25369.
4. K. Wang, Y.-H. Shi, H.-H. Li, H.-F. Wang, X.-Y. Li, H.-Z. Sun, X.-L. Wu, H.-M. Xie, J.-P. Zhang and J.-W. Wang, *Electrochimica Acta*, 2016, **215**, 267-275.
5. J. Li, W. Xu, C. Guo, M. Li and L. Zhang, *Electrochimica Acta*, 2018, **276**, 333-342.
6. Y. Tang and Y. Lu, *Chemical Engineering Journal*, 2019, **360**, 553-561.
7. Q. Li, Z. Liu, C. Wang, Y. Zhao and R. Che, *Small*, 2018, **14**, 1702574.
8. R. Zhang, X. Huang, D. Wang, T. K. A. Hoang, Y. Yang, X. Duan, P. Chen, L.-C. Qin and G. Wen, *Advanced Functional Materials*, 2018, **28**, 1705817.
9. W. Kang, D. Y. Yu, W. Li, Z. Zhang, X. Yang, T. W. Ng, R. Zou, Y. Tang, W. Zhang and C. S. Lee, *Nanoscale*, 2015, **7**, 10146.
10. S. Shi, M. Zhang, T. Deng, T. Wang and G. Yang, *Electrochimica Acta*, 2017, **246**, 1004-1015.
11. D. Wang, W. Zhou, R. Zhang, X. Huang, J. Zeng, Y. Mao, C. Ding, J. Zhang, J. Liu and G. Wen, *Journal of Materials Chemistry A*, 2018, **6**, 2974-2983.
12. X. Chen, Y. Zhang, H. Lin, P. Xia, X. Cai, X. Li, X. Li and W. Li, *Journal of Power Sources*, 2016, **312**, 137-145.

13. J. Xu, H. Zhang, R. Wang, P. Xu, Y. Tong, Q. Lu and F. Gao, *Langmuir*, 2018, **34**, 1242-1248.